SCIENTIFIC REPORTS
nature research

OPEN

Weak Antilocalization and Anisotropic Magnetoresistance as a Probe of Surface States in Topological $Bi_2Te_xSe_{3-x}$ Thin Films

Gregory M. Stephen[1*], Owen. A. Vail[2], Jiwei Lu[3], William A. Beck[2], Patrick J. Taylor[2] & Adam L. Friedman[1*]

Topological materials, such as the quintessential topological insulators in the Bi_2X_3 family (X = O, S, Se, Te), are extremely promising for beyond Moore's Law computing applications where alternative state variables and energy efficiency are prized. It is essential to understand how the topological nature of these materials changes with growth conditions and, more specifically, chalcogen content. In this study, we investigate the evolution of the magnetoresistance of $Bi_2Te_xSe_{3-x}$ for varying chalcogen ratios and constant growth conditions as a function of both temperature and angle of applied field. The contribution of 2D and 3D weak antilocalization are investigated by utilizing the Tkachov-Hankiewicz model and Hakami-Larkin-Nagaoka models of magnetoconductance.

In topological insulators (TIs), a finite band gap in the bulk is accompanied by metallic surface states with linear dispersion, resulting from band inversion[1,2]. These surface states have a variety of potential applications owing to their robustness resulting from topological protection, potentially high mobilities, and spin-momentum locking, making them ideal candidates for spin-transport[3–8]. In particular, devices for applications in advanced computing and logic beyond Moore's law have been envisioned[9–13].

Bi_2Se_3 and Bi_2Te_3 are prototypical TIs that have been widely studied in order to understand this vibrant class of materials[14–19]. This is because they are relatively simple to grow as thin films[20–22], and both possess a single Dirac point at accessible doping levels[23]. Despite the great amount of research into their topological nature, little work has been done to understand how changing concentrations with either Se or Te affect the overall topological properties. Insight into the nature of the conducting surface states as well as their robustness to chemical substitution is vital to effectively utilizing these materials. Further rationale for investigating $Bi_2Te_xSe_{3-x}$ alloys is that they offer robust Dirac dispersion for surface conduction combined with a path toward reduced bulk conductivity compared to their parent compounds at either x = 0 or 3[24]. Specifically, the Bi_2Te_2Se alloy represents a special line compound whose bulk conductivity is sufficiently low that surface and bulk transport may be distinguished[25]. The interest, therefore, is to obtain high quality epitaxial thin films that facilitate transport mediated by topological surface states distinct from bulk electronic states. Moreover, in order to use these materials in the proposed applications, the material properties must be optimized.

In this work, we perform magnetoresistance (MR) measurements on four Bi-based topological material films: Bi_2Se_3, Bi_2Te_3, and two films with a mixture of Se and Te under constant growth conditions. We observe the 2D weak anti-localization (WAL) indicative of topological materials and we explore anisotropic magnetoresistance effects. We find a strong angle-independent WAL contribution in Bi_2Se_3 resulting from 3D bulk states. 2D states arise as Te replaces Se, creating a $\sin\theta$ dependence to the WAL though also accompanied by an increasing classical MR background. However, these 2D states disappear in the pure Bi_2Te_3.

[1]Laboratory for Physical Sciences, 8050 Greenmead Dr., College Park, MD, 20740, United States. [2]Army Research Laboratory, 2800 Powder Mill Rd., Adelphi, MD, 20783, United States. [3]Department of Materials Science and Engineering, University of Virginia, Charlottesville, VA, 22904, United States. *email: gstephen@lps.umd.edu; afriedman@lps.umd.edu

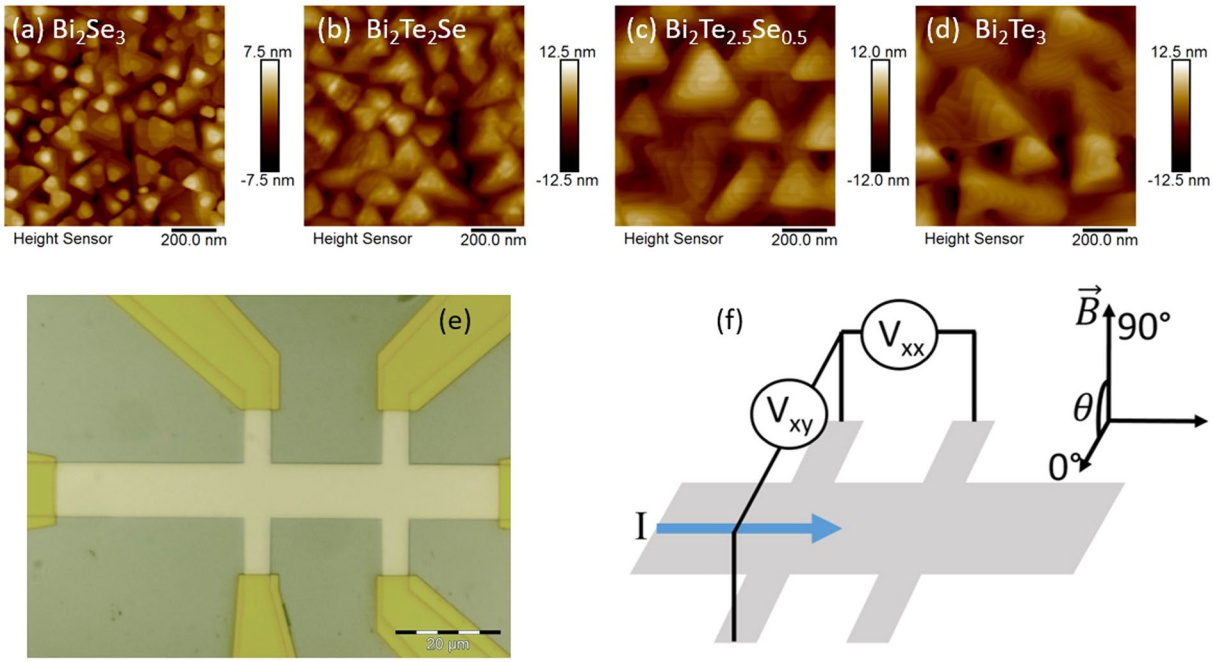

Figure 1. (**a–d**) AFM images of the four alloys used in this study. The surface height variation for these same films was between 15 nm for Bi_2Se_3 and 25 nm for Bi_2Te_3. (**e**) Optical image of one 10×20 µm hall bar. (**f**) Schematic of hall bar and magnetic field orientation.

Thin Film Growth and Device Fabrication

MBE growth of $Bi_2Te_xSe_{3-x}$ was performed on (001) semi-insulating GaAs. During MBE growth, the relative (Te + Se)/Bi beam-equivalent flux ratios for all epitaxial layers ranged from 15–20, and the nominal growth temperature was constant at 290 °C. For consistency, the thickness of all films was limited to 50 nm. The specific alloys that were obtained in this study include pure Bi_2Se_3 (x = 0), $Bi_2Te_2Se_1$ (x = 2), $Bi_2Te_{2.5}Se_{0.5}$ (x = 2.5) and pure Bi_2Te_3 (x = 3). X-ray, RHEED and TEM characterization confirmed high quality epitaxy throughout the alloy system with a sharp interface with the substrate. (see Supplemental Materials Figs. S5–7). Nonetheless, AFM analysis [Fig. 1(a–d)] of the highly specular films showed that the surface height varies between 15 nm for Bi_2Se_3 and 25 nm for Bi_2Te_3, similar to other MBE grown films in the literature[22,26,27]. This discrepancy is likely due to the highly polycrystalline nature of the films.

Mesoscopic Hall bars (10×20 µm^2, Fig. 1(e)) were defined lithographically with an argon plasma etch. While plasma is known to cause damage, the surface was protected by a 1.5 µm thick, spun-on layer of poly(methyl methacrylate) (PMMA) such that the edges of the mesa were sharp, and similar measurements using similar un-patterned films with pressed indium contacts showed similar carrier densities. Electron beam evaporated gold (150 nm) with a titanium adhesion layer (10 nm) provided Ohmic contact to the Hall bar. Gold wire bonds were affixed with a ball bonder using indium spheres without heating or ultrasonic agitation.

Magnetoresistance Measurements and Analysis

Magnetoresistance (MR) was measured for all four samples in a variable temperature cryostat set in a 1 T resistive magnet on a rotating platform. Sample measurement geometry was as shown in the schematic depicted in Fig. 1(f). For a majority of the measurements, the magnetic field is first applied in-plane with the film and perpendicular to the current direction, as indicated in the figure. The magnet is then incrementally rotated around the sample in the cryostat using the rotating platform such that the field is eventually out-of-plane with the sample. Other studies in the literature observed an anomalous negative magnetoresistance in Bi_2Se_3 when the magnetic field is both in-plane with the film and parallel to the applied current[28]. However, the negative component is expected to dominate at fields significantly higher than those used in our experiment. Nonetheless, we performed the measurement using this geometry on our samples as well and indeed observed similar results to the geometry shown in Fig. 1 (See Supplemental Materials, Fig. S1).

First, we measure mobility of all of the samples. Hall mobilities μ_{Hall} and carrier concentrations n were determined using the ordinary Hall effect $dR_{xy}/dB = 1/net$, where t is the sample thickness, e is the elementary electronic charge, and $\mu_{Hall} = 1/ne\rho$. The temperature dependence of the carrier concentrations and Hall mobilities are shown in Fig. 2. In Bi_2Se_3, n is nearly independent of temperature due to the semimetallic nature of the Dirac state, while n in Bi_2Te_3 has a strong exponential dependence due to the stronger influence of the bulk bandgap in the transport. Conversely, the mobility in Bi_2Te_3 and $Bi_2Te_{2.5}Se_{0.5}$ decreases inversely proportional to T, while the mobility in Bi_2Se_3 and Bi_2Te_2Se changes less with T. The strength of the decrease in the mobility with temperature relates to the amount of scattering within the material. For topologically protected states, the scattering should be reduced, thus maintaining a more constant mobility with temperature. The increase (decrease) in carrier

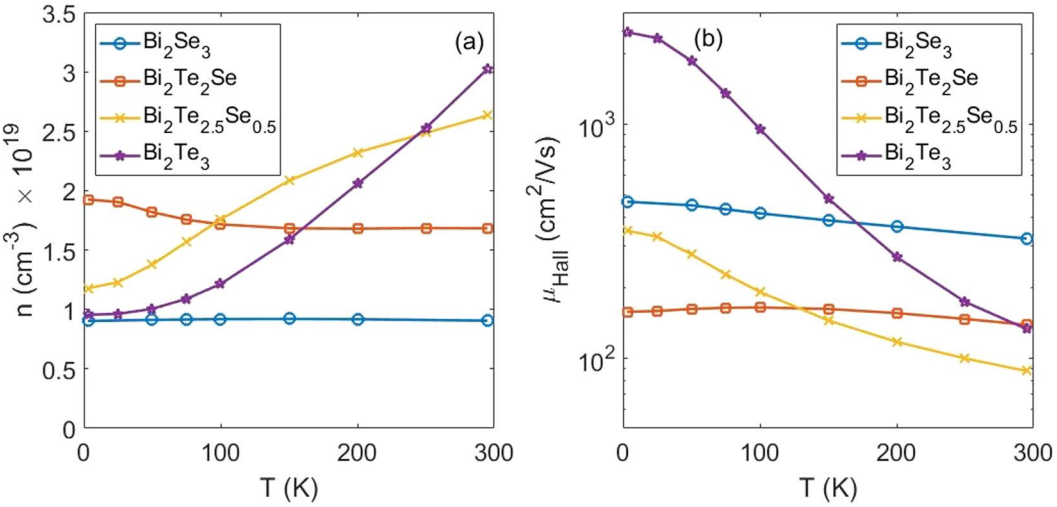

Figure 2. Carrier concentration (**a**) and mobility (**b**) versus temperature for the various Te concentrations. The large carrier concentration of 1019 cm-3 indicates these samples are heavily doped into the conduction band. However, the reduced mobility for the two intermediate samples suggests a stronger proportion of the conduction occurs in the surface. (See Supplemental Materials Fig. S8 for resistance versus temperature).

concentration (mobility) is consistent with the Bi_2Te_3 and $Bi_2Te_{2.95}Se_{0.05}$ samples having conventional conducting states, while the steadier mobility in Bi_2Se_3 and Bi_2Te_2Se is strong evidence of topological protection. The anomalous slight increase in mobility for Bi_2Te_2Se could result from ionized impurity scattering[29,30]. Our measured mobilities of 100–1000 cm^2/Vs correspond to mean free path on the order of 10 nm, corresponding to diffusive transport within our samples[6].

Figure 3 shows Magnetoconductance ($\Delta\sigma$) vs. Magnetic field for both in-plane and out-of-plane magnetic field for the samples that contained Se. Open circles in blue show the data for the in-plane applied magnetic field, while the dashed lines of the same color show the fits to the models, discussed below. Likewise, red "x" marks show the data for the out-of-plane magnetic field and the red dashed line shows the fits. The pure Bi_2Te_3 sample show a very weak WAL cusp, however the strength of the quadratic background drastically increases the uncertainty in the fitting. Further information can be found in the Supplemental Materials Figs. S3, S4. At 3 K, weak antilocalization (WAL) is observed with a magnetic field applied both in-plane (0°) and out-of-plane (90°), persisting up to 50 K (see Supplemental Materials Fig. S3). For an out-of-plane magnetic field B, the Hikami-Larkin-Nagaoka model for 2D WAL in the strong spin-orbit coupling limit gives the change in conductance as

$$\frac{\Delta\sigma_{xx,\perp}}{\sigma_0} = \frac{\alpha e^2}{2\pi h}\left[\psi\left(\frac{B_\perp}{B}+\frac{1}{2}\right) - \ln\left(\frac{B_\perp}{B}\right)\right] \tag{1a}$$

$$B_\perp = \frac{\hbar}{2eL^2}, \tag{1b}$$

where ψ is the Digamma function, L is the coherence length, and e and h are the electron charge and Plank constant, respectively[31–33]. For Dirac states, the coefficient α is expected to be 1/2 for each Dirac cone[34]. As is evident in Fig. 3, the model fits the data well. From the fits, we extract the localization length and α. The 3 samples give values of $\alpha = 0.43$, 0.50, and 0.42 for Bi_2Se_3, Bi_2Te_2Se, and $Bi_2Te_{2.5}Se_{0.5}$, respectively. This range is consistent with literature and indicates 2D topological surface transport[14,34].

A linear background is subtracted for the Bi_2Se_3 and Bi_2Te_2Se samples, and a quadratic background for the $Bi_2Te_{2.5}Se_{0.5}$. The character of the backgrounds is derived from the MR behavior up to 9 T (see Supplemental Materials Fig. S4). Similar linear magnetoresistance has previously been observed in these materials, likely arising from the polycrystalline nature of the films, observed here in the AFM images in Fig. 1 [35–39]. As evidenced by the magnetoresistance data, the quadratic contribution decreases as Te is replaced with Se. The normalization of using $[R(B) - R(0)]/R(0)$ shows the relative contribution of the two component independent of the absolute resistance.

Unusually, TIs exhibit WAL with an applied in-plane field as well. This behavior can partially be explained by WAL originating from 3D states due to high spin-orbit coupling in the bulk, where the effect is independent of field angle[40]. Additionally an in-plane contribution for 2D states is hypothesized to arise due to a unique hexagonal warping of the surface state energy spectrum at all applied magnetic field angles. In a parallel magnetic field, the magnetic flux through the surface states decays exponentially up to a certain skin depth, defining an effective surface state depth. The magnetoconductance in a TI with an in-plane magnetic field is derived by Tkachov and Hankiewicz in ref. [41] to be

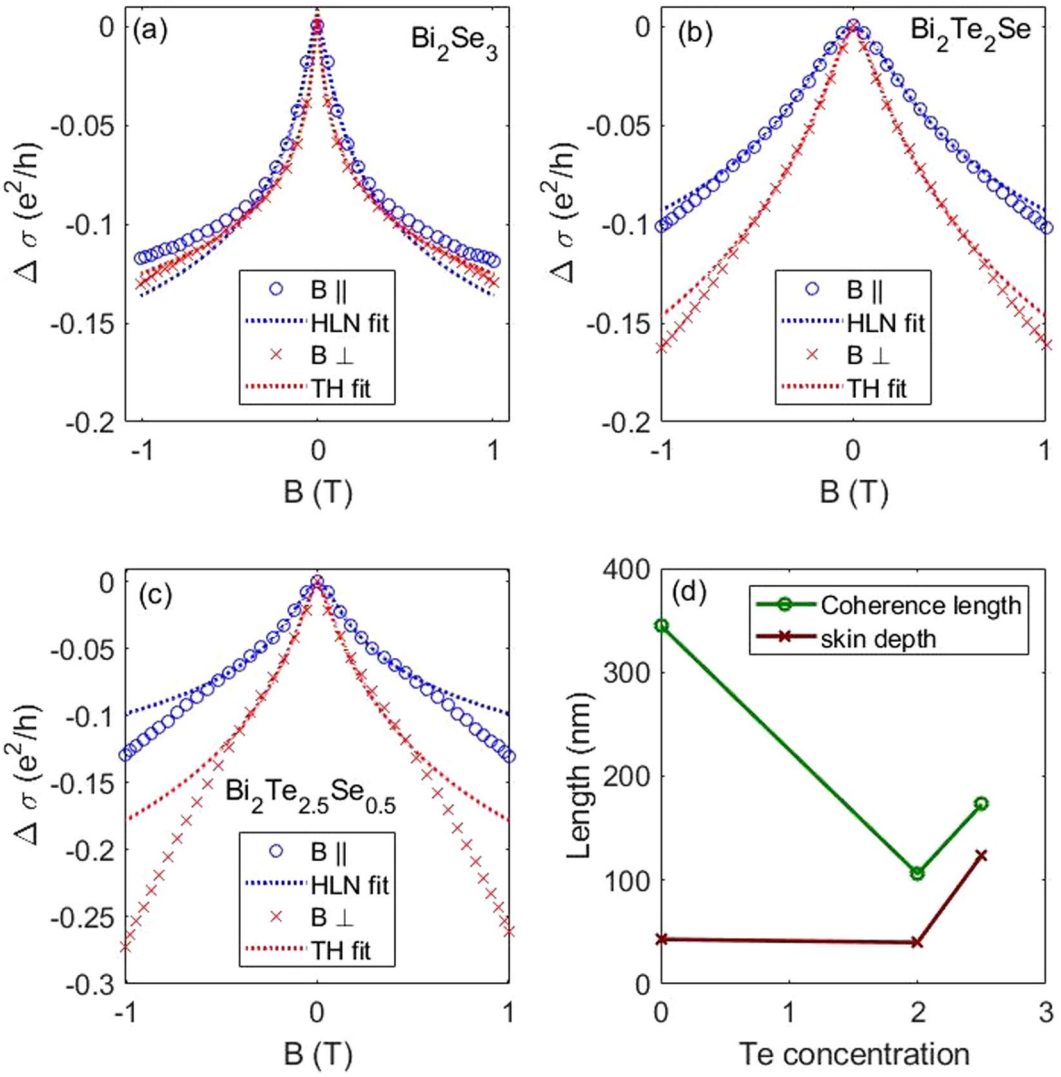

Figure 3. Magnetoconductance ($\Delta\sigma$) vs. Magnetic field for both in-plane and out-of-plane magnetic fields and the Hikami-Larkin-Nagaoka (HLN) and Tkachov-Hankiewicz (TH) fits with a linear background term (quadratic for x = 2.5). Fits at 3 K for the (**a**) Bi_2Se_3, (**b**) Bi_2Te_2Se, and (**c**) $Bi_2Te_{2.5}Se_{0.5}$ samples for in-plane and out-of-plane fields. WAL was extremely weak compared to the much stronger quadratic background for Bi_2Te_3. Thus, it is not included in these plots. (**d**) Extracted coherence length from the HLN fit is used in the TH fit to calculate the skin depth.

$$\frac{\Delta\sigma_{xx,\parallel}}{\sigma_0} = -\frac{e^2}{2\pi h}\ln\left(1+\frac{B^2}{B_\parallel^2}\right) \tag{2a}$$

$$B_\parallel = \frac{2L}{\lambda}B_\perp = \frac{\hbar}{\lambda eL}, \tag{2b}$$

where, λ is the effective surface state skin depth. For a purely 2D surface state ($\lambda = 0$), the argument of the log term reduces to 1, eliminating the change in magnetoconductance for an in-plane magnetic field. The existence of in-plane WAL requires a finite skin depth for the surface states, as well as a wide enough field range or small enough λ/L such that the effect is observably non-quadratic. For sufficiently large values of λ/L, the in-plane magnetoconductance will be quadratic over a large magnetic field range, in which case the in-plane WAL behavior could be identified as trivial anisotropic magnetoresistance (AMR). The in-plane quadratic MR has previously been observed in Bi_2Te_3[40]. However, to our knowledge, this is the first application of the Tkachov-Hankiewicz model to explain in-plane magnetoconductance data apart from the authors' original culling of data available in the literature at the time of their derivation. As observed in Fig. 3, the data and model are in excellent agreement.

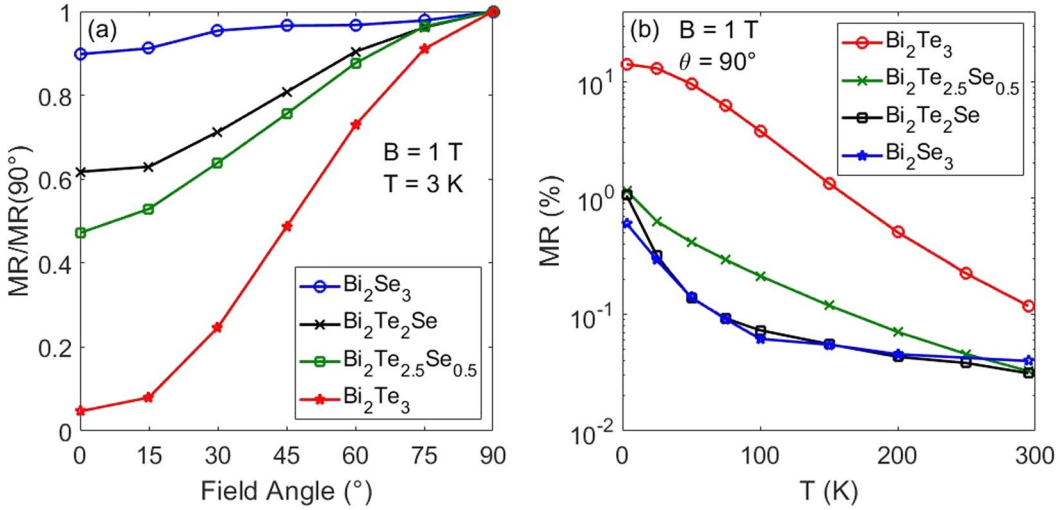

Figure 4. (**a**) MR vs. field angle, normalized to the value at $\theta = 90°$. Bi_2Te_3 nearly follows a $\sin\theta$ dependence while Bi_2Se_3 is nearly constant with angle, with the Se, Te mixed samples decreasing between the extremes. (**b**) MR vs. Temperature. The Se containing samples decrease more quickly than the pure Bi_2Te_3 due to the rapid disappearance of WAL.

From the fits, values for the coherence length and effective surface state skin depth are extracted and shown in Fig. 3(d). The coherence length (skin depth) decreases (increases) with increasing Te concentration, with the WAL effect disappearing in Bi_2Te_3. The measured effective skin depth for each sample is on the order of the surface height roughness as seen in Fig. 1(a–d), which is much greater than the expected ~4 nm for the topological surface state skin depth from literature[42,43]. As this value is measure across a macroscopic sample, the effective surface depth is a convolution of the depth of the surface state and the roughness of the sample. Additionally, defects near the surface of the topological material can lead to an increase in the skin depth[44]. These samples are heavily electron doped ($n \approx 10^{19}$ cm^{-3}) which, along with the relative complexity of the band structure for Bi_2Te_3 relative to Bi_2Se_3, provides an explanation for the disappearance of the surface states. Bi_2Se_3 has a bulk bandgap of 0.3 eV, compared to 0.1 eV for Bi_2Te_3[45,46]. Additionally, the Dirac point in Bi_2Te_3 lies below the maximum of the bulk valence band while the Dirac point in Bi_2Se_3 lies above the bulk valence band. The larger band gap and less proximity of bulk states to the Dirac point allow Bi_2Se_3 to maintain its topological behavior over a wider range of dopings than Bi_2Te_3. In addition to the decrease in WAL signal, Te substitution is accompanied by an increase in the Hall mobility, owing to a Fermi energy firmly in the conduction band. Based on band structure calculations from the literature it is apparent that bulk bands are closer to the dirac point in Bi_2Te_3 than in Bi_2Se_3. Thus, the high carrier concentration in our samples has likely moved the Fermi level far enough into the bulk as to reduce the relative contribution of the surface states[18,23,45]. We expect the alloyed compositions to have band structures that are some linear combination of the Bi_2Se_3 and Bi_2Te_3 bands. From the measured effective penetration depth, we also expect some coupling of surface states on the top and bottom of the film.

From the fits, we see a coherent picture of the development of the topological states as Se is replaced by Te, with λ being on the order of the sample roughness. This observation demonstrates the importance of film surface roughness to obtaining surface-pinned topological states that mix minimally with the bulk. At low temperature, there is a competition between the WAL from the surface states and a low field quadratic background. As the mobility at 3 K increases significantly in pure Bi_2Te_3 compared to the other samples, the relative size of the WAL cusp decreases leading to the near disappearance of WAL in Bi_2Te_3. A small cusp is visible, though overwhelmed by a quadratic background which precludes fitting to the Hikami-Larkin-Nagaoka model. The lack of angular dependence in the WAL signal from Bi_2Se_3 indicates a 3D origin, while the stronger theta-dependence in the alloyed samples indicates some 2D surface contribution.

In various other studies on Bi_2Se_3, a negative longitudinal magnetoresistance is observed when the field is applied along the current, often attributed to the chiral anomaly[47–49]. We do not observe this effect over the measured field range as the negative magnetoresistance effect is overwhelmed by the WAL at low fields. The in-plane WAL of the Tkachov-Hankiewicz model still occurs as it depends on the relative direction of the field to the surface, not the current direction. Thus, we consider the geometry that we used to be representative of the total angle-dependent field behavior at small fields.

MR was also measured as the angle between field and sample is varied from 0° (in-plane) to 90° (out-of-plane). The change at B = 1 T as a function of angle and normalized to the value at 90° is plotted in Fig. 4(a) (see Supplemental Materials Fig. S2 for additional data). In conventional materials, anisotropic magnetoresistance arises from coupling to the out-of-plane magnetic field, leading to a dependence on B $\sin\theta$[50–53]. However, the increased θ-dependence of WAL for increasing Te contribution, up to x = 2.5, suggests a stronger surface contribution in $Bi_2Te_{2.5}Se_{0.5}$ than in Bi_2Se_3.

Figure 4(b) shows the temperature dependence of the MR. As expected, the change in MR decreases with increasing temperature. The samples that show WAL have a cusp that broadens with T and develops into fully quadratic MR by 100 K. The MR at 1 T is plotted vs. temperature in Fig. 4(b). The rapid decrease in MR in the Bi_2Se_3 and Bi_2Te_2Se samples is due to the disappearance of WAL, while Bi_2Te_3 decreases steadily from the steadily decreasing mobility. The WAL decrease follows nearly the same divergent dependence in T as does $\Delta\sigma(B)$ due to the temperature dependence of the coherence length ($L \sim T^{-1}$) and the divergence of $\psi(x)$. $Bi_2Te_{2.5}Se_{0.5}$ decreases slower than the other Se-containing samples due to a relatively stronger background MR.

Conclusion

In conclusion, we have demonstrated non-trivial AMR in Bi_2Se_3 arising from a non-zero skin depth of the topological surface states. As the Se is substituted for Te, the surface states are overshadowed by bulk conduction, leading to more conventional behavior in Bi_2Te_3. This results in distinctive weak antilocalization and non-trivial anisotropic magnetoresistance in Se-containing samples which does not appear in Bi_2Te_3. The Tkachov-Hankiewicz coupled with the Hikami-Larkin-Nagaoka model provides a straightforward means of measuring both the coherence length and characterizing the quality of the surface states through the effective skin depth. We have also demonstrated that careful investigation of the low field in-plane MR in topological materials can provide valuable insight into surface states and sample quality, information that will prove vital to best utilizing topological surface states and optimizing film growths.

Received: 19 December 2019; Accepted: 28 February 2020;
Published online: 16 March 2020

References

1. Hasan, M. Z. & Kane, C. L. Colloquium: Topological insulators. *Rev. Mod. Phys.* **82**, 3045–3067 (2010).
2. Qi, X.-L. & Zhang, S.-C. The quantum spin Hall effect and topological insulators. *Phys. Today* **63**, 33–38 (2010).
3. Li, C. H. *et al*. Electrical detection of charge-current-induced spin polarization due to spin-momentum locking in Bi_2Se_3. *Nat. Nanotechnol.* **9**, 218–224 (2014).
4. Liu, L. *et al*. Spin-polarized tunneling study of spin-momentum locking in topological insulators. *Phys. Rev. B* **91**, 235437 (2015).
5. Narendra, N., Norouzzadeh, P., Vashaee, D. & Kim, K. W. Doping induced enhanced density of states in bismuth telluride. *Appl. Phys. Lett.* **111**, 232101 (2017).
6. Butch, N. P. *et al*. Strong surface scattering in ultrahigh-mobility Bi_2Se_3 topological insulator crystals. *Phys. Rev. B* **81**, 241301 (2010).
7. Neupane, M. *et al*. Observation of a three-dimensional topological Dirac semimetal phase in high-mobility Cd3As2. *Nat. Commun.* **5**, 3786 (2014).
8. Shekhar, C. *et al*. Extremely large magnetoresistance and ultrahigh mobility in the topological Weyl semimetal candidate NbP. *Nat. Phys.* **11**, 645–649 (2015).
9. Xiu, F. *et al*. Manipulating surface states in topological insulator nanoribbons. *Nat. Nanotechnol.* **6**, 216–221 (2011).
10. Fan, Y. *et al*. Magnetization switching through giant spin-orbit torque in a magnetically doped topological insulator heterostructure. *Nat. Mater.* **13**, 699–704 (2014).
11. Semenov, Y. G., Li, X. & Kim, K. W. Tunable photogalvanic effect on topological insulator surfaces via proximity interactions. *Phys. Rev. B* **86**, 201401 (2012).
12. Duan, X., Li, X.-L., Li, X., Semenov, Y. G. & Kim, K. W. Highly efficient conductance control in a topological insulator based magnetoelectric transistor. *J. Appl. Phys.* **118**, 224502 (2015).
13. Pesin, D. & MacDonald, A. H. Spintronics and pseudospintronics in graphene and topological insulators. *Nat. Mater.* **11**, 409–416 (2012).
14. Jing, Y. *et al*. Weak antilocalization and electron-electron interaction in coupled multiple-channel transport in a Bi_2Se_3 thin film. *Nanoscale* **8**, 1879–1885 (2016).
15. Kong, D. *et al*. Few-layer nanoplates of Bi_2Se_3 and Bi_2Te_3 with highly tunable chemical potential. *Nano Lett.* **10**, 2245–2250 (2010).
16. Steinberg, H., Laloë, J.-B., Fatemi, V., Moodera, J. S. & Jarillo-Herrero, P. Electrically tunable surface-to-bulk coherent coupling in topological insulator thin films. *Phys. Rev. B* **84**, 233101 (2011).
17. Steinberg, H., Gardner, D. R., Lee, Y. S. & Jarillo-Herrero, P. Surface state transport and ambipolar electric field effect in Bi 2Se3 nanodevices. *Nano Lett.* **10**, 5032–5036 (2010).
18. Chen, Y. L. *et al*. Experimental Realization of a Three-Dimensional Topological Insulator, Bi_2Te_3. *Science* **325**, 178–181 (2009).
19. Chang, C.-Z. *et al*. High-precision realization of robust quantum anomalous Hall state in a hard ferromagnetic topological insulator. *Nat. Mater.* **14**, 473–477 (2015).
20. He, L. *et al*. Epitaxial growth of Bi_2Se_3 topological insulator thin films on Si (111). *J. Appl. Phys.* **109**, 103702 (2011).
21. Ota, J. R., Roy, P., Srivastava, S. K., Popovitz-Biro, R. & Tenne, R. A simple hydrothermal method for the growth of Bi_2Se_3 nanorods. *Nanotechnology* **17**, 1700–1705 (2006).
22. Zeng, Z. *et al*. Molecular beam epitaxial growth of Bi_2Te_3 and Sb_2Te_3 topological insulators on GaAs (111) substrates: a potential route to fabricate topological insulator p-n junction. *AIP Adv.* **3**, 072112 (2013).
23. Hor, Y. S., Checkelsky, J. G., Qu, D., Ong, N. P. & Cava, R. J. Superconductivity and non-metallicity induced by doping the topological insulators Bi_2Se_3 and Bi_2Te_3. *J. Phys. Chem. Solids* **72**, 572–576 (2011).
24. Kushwaha, S. K. *et al*. Sn-doped Bi1.1Sb0.9Te2S bulk crystal topological insulator with excellent properties. *Nat. Commun.* **7**, 11456 (2016).
25. Kapustin, A. A., Stolyarov, V. S., Bozhko, S. I., Borisenko, D. N. & Kolesnikov, N. N. Surface origin of quasi-2D Shubnikov–de Haas oscillations in Bi_2Te_2Se. *J. Exp. Theor. Phys.* **121**, 279–288 (2015).
26. Liu, X. *et al*. Characterization of Bi_2Te_3 and Bi_2Se_3 topological insulators grown by MBE on (001) GaAs substrates. *J. Vac. Sci. Technol. B* **30**, 02B103 (2012).
27. Levy, I., Garcia, T. A., Shafique, S. & Tamargo, M. C. Reduced twinning and surface roughness of Bi_2Se_3 and Bi_2Te_3 layers grown by molecular beam epitaxy on sapphire substrates. *J. Vac. Sci. Technol. B* **36**, 02D107 (2018).
28. Wiedmann, S. *et al*. Anisotropic and strong negative magnetoresistance in the three-dimensional topological insulator Bi_2Se_3. *Phys. Rev. B* **94**, 081302 (2016).
29. Long, D. & Myers, J. Ionized-Impurity Scattering Mobility of Electrons in Silicon. *Phys. Rev.* **115**, 1107–1118 (1959).
30. Chattopadhyay, D. & Queisser, H. J. Electron scattering by ionized impurities in semiconductors. *Rev. Mod. Phys.* **53**, 745–768 (1981).
31. Hikami, S., Larkin, A. I. & Nagaoka, Y. Spin-Orbit Interaction and Magnetoresistance in the Two Dimensional Random System. *Prog. Theor. Phys.* **63**, 707–710 (1980).
32. Bergmann, G. Measurement of the Magnetic Scattering Time by Weak Localization. *Phys. Rev. Lett.* **49**, 162–164 (1982).

33. Assaf, B. A. *et al*. Quantum coherent transport in SnTe topological crystalline insulator thin films. *Appl. Phys. Lett.* **105**, 102108 (2014).
34. Bao, L. *et al*. Weak Anti-localization and Quantum Oscillations of Surface States in Topological Insulator Bi_2Se_2Te. *Sci. Rep.* **2**, 726 (2012).
35. Johnson, H. G., Bennett, S. P., Barua, R., Lewis, L. H. & Heiman, D. Universal properties of linear magnetoresistance in strongly disordered MnAs-GaAs composite semiconductors. *Phys. Rev. B* **82**, 085202 (2010).
36. Abrikosov, A. A. Quantum linear magnetoresistance. *Europhys. Lett.* **49**, 789–793 (2000).
37. Assaf, B. A. *et al*. Linear magnetoresistance in topological insulator thin films: Quantum phase coherence effects at high temperatures. *Appl. Phys. Lett.* **102**, 012102 (2013).
38. Parish, M. M. & Littlewood, P. B. Classical magnetotransport of inhomogeneous conductors. *Phys. Rev. B* **72**, 094417 (2005).
39. Friedman, A. L. *et al*. Quantum linear magnetoresistance in multilayer epitaxial graphene. *Nano Lett.* **10**, 3962–3965 (2010).
40. He, H.-T. *et al*. Impurity Effect on Weak Antilocalization in the Topological Insulator Bi_2Te_3. *Phys. Rev. Lett.* **106**, 166805 (2011).
41. Tkachov, G. & Hankiewicz, E. M. Weak antilocalization in HgTe quantum wells and topological surface states: Massive versus massless Dirac fermions. *Phys. Rev. B* **84**, 035444 (2011).
42. Zhang, F., Kane, C. L. & Mele, E. J. Surface states of topological insulators. *Phys. Rev. B* **86**, 081303 (2012).
43. Vidal, F. *et al*. Photon energy dependence of circular dichroism in angle-resolved photoemission spectroscopy of Bi_2Se_3 Dirac states. *Phys. Rev. B* **88**, 241410 (2013).
44. Sacksteder, V., Ohtsuki, T. & Kobayashi, K. Modification and control of topological insulator surface states using surface disorder. *Phys. Rev. Appl.* **3**, 064006 (2015).
45. Zhang, H. *et al*. Topological insulators in Bi_2Se_3, Bi_2Te_3 and Sb_2Te_3 with a single Dirac cone on the surface. *Nat. Phys.* **5**, 438–442 (2009).
46. Yazyev, O. V., Moore, J. E. & Louie, S. G. Spin Polarization and Transport of Surface States in the Topological Insulators Bi_2Se_3 and Bi_2Te_3 from First Principles. *Phys. Rev. Lett.* **105**, 266806 (2010).
47. He, H. T. *et al*. Disorder-induced linear magnetoresistance in (221) topological insulator Bi_2Se_3 films. *Appl. Phys. Lett.* **103**, 031606 (2013).
48. Wang, J. *et al*. Anomalous anisotropic magnetoresistance in topological insulator films. *Nano Res.* **5**, 739–746 (2012).
49. Assaf, B. A. *et al*. Negative Longitudinal Magnetoresistance from the Anomalous N=0 Landau Level in Topological Materials. *Phys. Rev. Lett.* **119**, 106602 (2017).
50. Kandala, A., Richardella, A., Kempinger, S., Liu, C.-X. & Samarth, N. Giant anisotropic magnetoresistance in a quantum anomalous Hall insulator. *Nat. Commun.* **6**, 7434 (2015).
51. Vašek, P. *et al*. Anisotropic magnetoresistance of GaMnAs ferromagnetic semiconductors. *J. Supercond. Nov. Magn.* **23**, 1161–1163 (2010).
52. Huang, H. *et al*. Giant anisotropic magnetoresistance and planar Hall effect in $Sr_{0.06}$ Bi_2Se_3. *Appl. Phys. Lett.* **113**, 222601 (2018).
53. Li, H., Wang, H.-W., He, H., Wang, J. & Shen, S.-Q. Giant anisotropic magnetoresistance and planar Hall effect in the Dirac semimetal Cd_3As_2. *Phys. Rev. B* **97**, 201110 (2018).

Acknowledgements

The authors gratefully acknowledge critical assistance from LPS support staff including G. Latini, J. Wood, R. Brun, P. Davis, and D. Crouse. The authors gratefully acknowledge support from the Applied Research for the Advancement of Priorities program of the Office of the Secretary of Defense.

Author contributions

G.M.S. and A.L.F. devised the experiments, analyzed the data, and wrote the manuscript. G.M.S. performed the low-field and Hall measurements. O.A.V. fabricated the devices and took the high-field data. J.L. performed the AFM analysis. W.A.B. performed Hall and carrier analysis. P.J.T. grew the samples and took XRD, RHEED, and TEM data. A.L.F. designed and built the low-field measurement apparatus. All authors reviewed the manuscript.

Competing interests

The authors declare no competing interests.

Additional information

Supplementary information is available for this paper at https://doi.org/10.1038/s41598-020-61672-1.

Correspondence and requests for materials should be addressed to G.M.S. or A.L.F.

Reprints and permissions information is available at www.nature.com/reprints.

Publisher's note Springer Nature remains neutral with regard to jurisdictional claims in published maps and institutional affiliations.